MEDS Clinical Medicine (2024)
Clausius Scientific Press, Canada

DOI: 10.23977/medsc.2024.050521
ISSN 2616-1907 Vol. 5 Num. 5

Research on the Subthalamic Nucleus Identification Algorithm Based on LFP Signals

Mingcai Yao[a,*], Dechun Zhao[b,*], Keji Zhang, Ziqiong Wang

School of Life and Health Information, Chongqing University of Posts and Telecommunications, Chongqing, 400065, China
[a]2521529609@qq.com, [b]zhaodc@cqupt.edu.cn
**Corresponding author*

Keywords: Deep Brain Stimulation; Local Field Potential; Multi-scale; Residual Neural Network; Attention Mechanism

Abstract: Deep Brain Stimulation (DBS) has become an effective treatment for neurological disorders such as Parkinson's Disease (PD). During DBS surgery, brain signals at different depths are recorded through electrodes to accurately determine the electrode's implantation position and depth. Among these signals, Local Field Potentials (LFPs) reflect the synchronized activity of neuronal populations in specific brain regions, which is closely associated with the pathological mechanisms of Parkinson's disease. This study proposes an improved model based on Residual Neural Network (ResNet). In this model, a Residual Shrinkage Module is embedded into the residual block, and a soft threshold function is introduced to effectively suppress noise interference in the signals. Additionally, the model incorporates multi-scale convolution paths by constructing three independent DR-ResNet branches, each using different-sized convolution kernels to comprehensively capture multi-scale features in the LFP signals. Furthermore, an attention mechanism is applied to fuse and enhance the extracted features, thereby improving the accuracy of signal classification. Cross-validation results on the publicly available dataset from the University of Oxford demonstrate that the improved model achieves a classification accuracy of 94.67%, with an F1 score of 94.58%, showcasing strong robustness and superior classification performance.

1. Introduction

Parkinson's Disease (PD) is the second most common neurodegenerative disorder after Alzheimer's disease [1], primarily affecting individuals over the age of 60. Symptoms include cognitive impairment, autonomic dysfunction, sleep disturbances, and depression [2, 3]. The pathological features of PD include degeneration of the substantia nigra and a reduction in neurons of the nigrostriatal pathway, leading to resting tremor, rigidity, and bradykinesia [4].

The treatment options for Parkinson's Disease (PD) include medication and Deep Brain Stimulation (DBS). Long-term medication use may lead to complications, while DBS regulates neural activity by stimulating the internal globus pallidus (GPi) and subthalamic nucleus (STN), improving motor symptoms and quality of life [5-7]. The key to DBS surgery lies in microelectrode recording, electrode implantation, and precise stimulation of the target area, which effectively alleviates

symptoms [7]. STN-based DBS has become the mainstream treatment for PD [8], but accurate electrode placement is crucial [9, 10], as improper placement can lead to side effects or inadequate control [11]. Research shows that incorrect electrode placement is the primary reason for 48.5% of revisions in neurostimulation treatments [12], and 40% of patients experience poor post-operative outcomes[13,14]. Therefore, developing efficient electrode optimization methods to reduce surgery time and reliance on the physician's experience is key to improving treatment success rates and long-term outcomes.

Microelectrode recording (MER) is a key technology for target localization and optimal trajectory selection during DBS surgery, providing real-time signal information by recording neuronal activity. Linxia et al. [15] proposed using 2D time-series images and GASF images combined with deep fusion networks for automatic signal classification. Li C et al. [16] developed an amplitude-frequency perception deep fusion network for STN-DBS electrode optimization. Lei Cao et al. [17] used genetic algorithms to extract MER time-series features and optimize clustering. Maxime Peralta et al. [18] employed the SepaConvNet model for precise STN localization. K.A. Ciecierski et al. [19] designed a brain activity-based decision support system, incorporating an attention mechanism network for electrode classification. However, MER faces limitations such as signal complexity and noise interference [20-23].

In recent years, Local Field Potentials (LFPs) have been closely associated with PD motor symptoms [24, 25], reflecting the activity of large neuronal populations. Studies have shown the safety of LFPs in PD treatment and their contribution to adaptive DBS (aDBS) [26]. Ozturk et al. [27] found that LFPs offer higher accuracy in localizing the STN compared to MER. Mohamed Hosny et al. [28] proposed the CNN-GA-KNN model to improve classification accuracy, and later used an integrated learning model combining LFPs with wavelet packets, achieving a classification accuracy of 89.49% [29]. They also implemented a recursive convolutional neural network, achieving a localization accuracy of 96.79% [30].

This paper proposes a model based on multi-scale residual convolutional neural networks for recognizing and classifying LFP signals. The model is capable of capturing features at different scales and adapting to the dynamic changes of LFP signals in both frequency and amplitude. Additionally, the model inherits the advantages of residual connections in residual networks, mitigating the vanishing gradient problem in deep networks. To further optimize the network structure, the model introduces a channel-shared adaptive threshold shrinkage technique, which uniformly processes data across different channels. This design effectively reduces the number of network parameters, enhances computational efficiency, and ensures the model's generalization ability in multi-channel signal processing.

2. Methods

In traditional CNNs, convolutional kernels with a single scale may struggle to fully capture multi-scale feature information. To address this issue more effectively, this paper proposes a novel model based on Residual Neural Network (ResNet), embedding a Residual Shrinkage Module within the residual block. By introducing a soft threshold function, the model effectively suppresses noise interference in the signals. Combined with multi-scale convolution paths, the model consists of three independent DR-ResNet branches, each using convolution kernels of different sizes to capture multi-scale features in the LFP signals. Additionally, the attention mechanism is applied to fuse and enhance the extracted features. The model structure is shown in Figure 1.

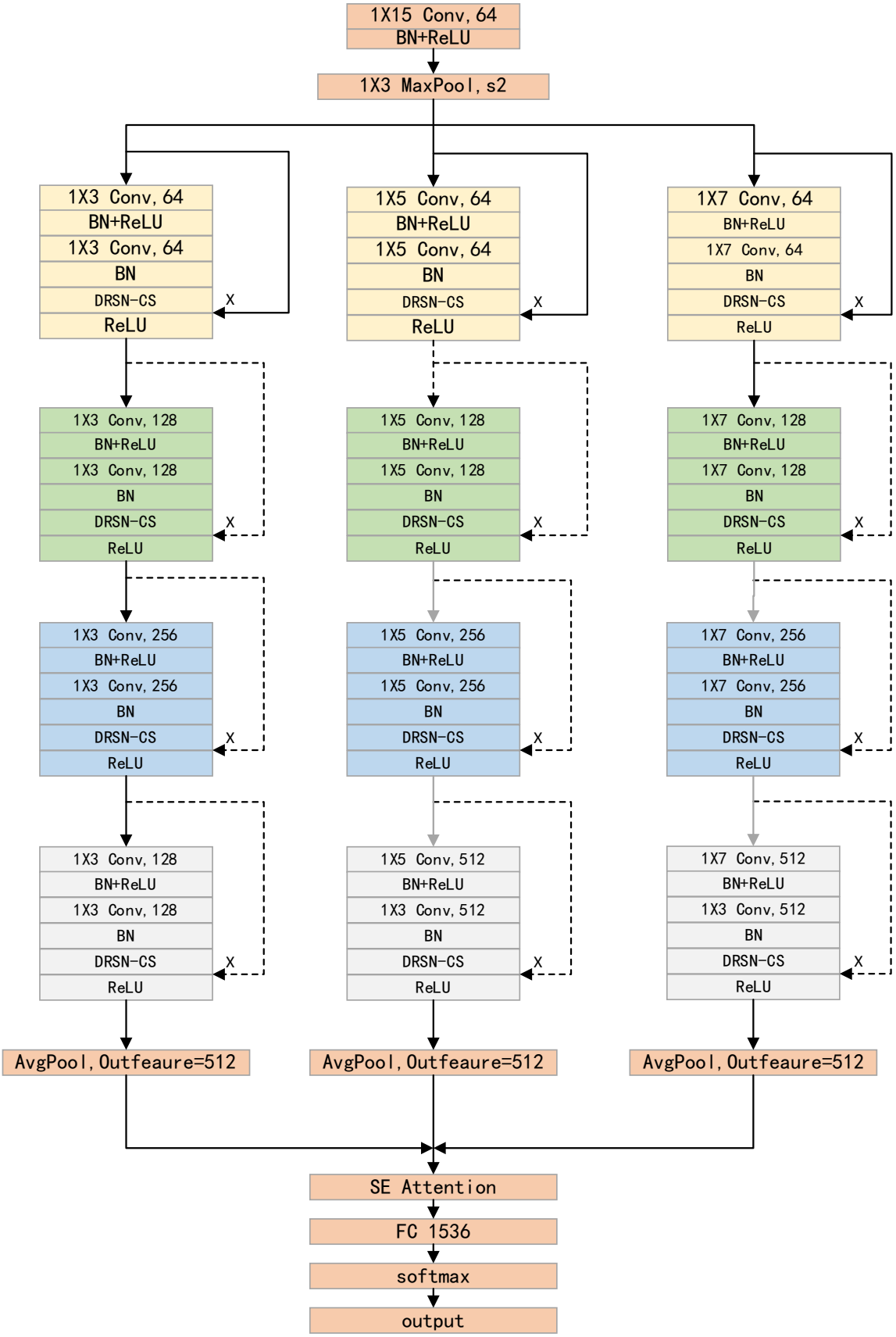

Figure 1: Model Structure Diagram

2.1 Residual Shrinkage Module

2.1.1 Soft Threshold

The soft threshold is a function that shrinks the input data towards zero, as shown in Equation (3). It is commonly used in signal denoising algorithms.

$$y = \begin{cases} x - \tau & x > \tau \\ 0 & -\tau \le x \le \tau \\ x + \tau & x < -\tau \end{cases} \tag{1}$$

Here, x represents the input features, y represents the output features, and τ is the threshold. The threshold must be a positive number and should not be too large. If the threshold is greater than the absolute value of all input features, the output feature y will be zero. In this case, the soft thresholding would lose its significance. The derivative of the soft thresholding function is given by the following formula:

Let x be the input features, y be the output features, and τ be the threshold. The threshold τ must be a positive number and should not be too large. If τ exceeds the absolute values of all input features x, the output feature y will approach zero, rendering the soft thresholding operation meaningless. Additionally, the derivative of the soft thresholding function is given by Equation (4).

$$\frac{\partial y}{\partial x} = \begin{cases} 1 & x > \tau \\ 0 & -\tau \le x \le \tau \\ 1 & x < -\tau \end{cases} \tag{2}$$

It can be seen that the derivative of the soft thresholding function is either zero or one. Both the soft thresholding function and its derivative are shown in Figure 2. This property is similar to that of the ReLU activation function, and therefore, the soft thresholding function helps prevent the vanishing and exploding gradient problems.

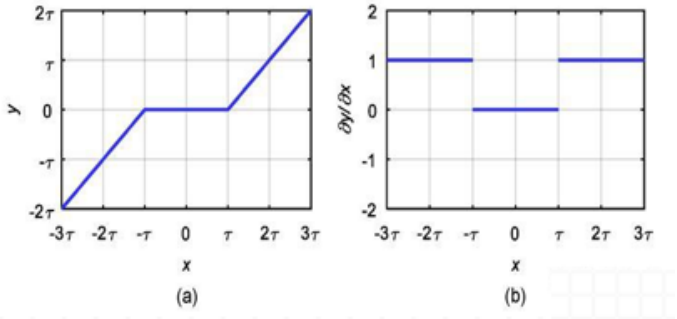

Figure 2: Soft Threshold and Its Derivative

2.1.2 DRSN-CS

Residual Shrinkage Module: The core idea of DRSN is to combine the residual learning mechanism to retain the original features of the input signal, while utilizing a shrinkage unit to denoise the features. Traditional ResNet learns high-level features of the signal through residual blocks and adds the input directly to the output layer via "skip connections." This structure directly transmits the input to the deeper layers, effectively alleviating the vanishing gradient problem in the network and accelerating the convergence speed.

The DRSN-CS module (see Figure 3) adds a small sub-network for adaptive threshold setting based on the traditional residual module. After passing through the sigmoid function, the threshold is constrained to a value between 0 and 1. Therefore, the threshold is always positive and appropriate, preventing the output from becoming zero and ensuring the effectiveness of the model.

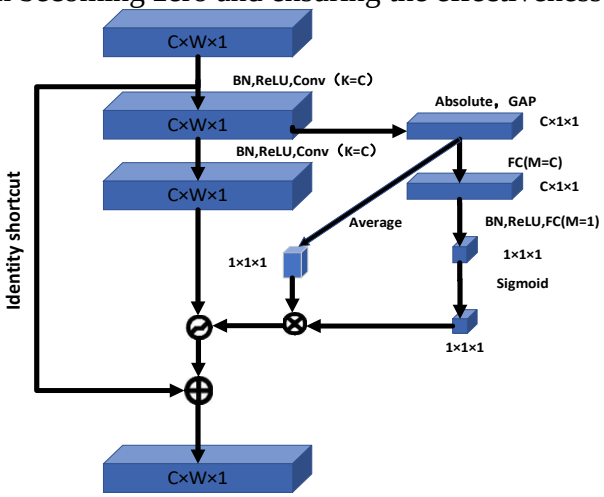

Figure 3: DRSN Module

2.2 Improved Residual Module: DR-ResNet

The DR-ResNet model combines the residual learning mechanism of ResNet with the denoising function of DRSN, as shown in Figure 4. This module retains the advantages of ResNet in efficient feature extraction, while enhancing the network's robustness and accuracy through noise suppression, making it more suitable for handling complex physiological signal classification tasks. With this design, the improved residual module can effectively remove noise while preserving key signal features, and it supports efficient training and fast convergence of deep networks.

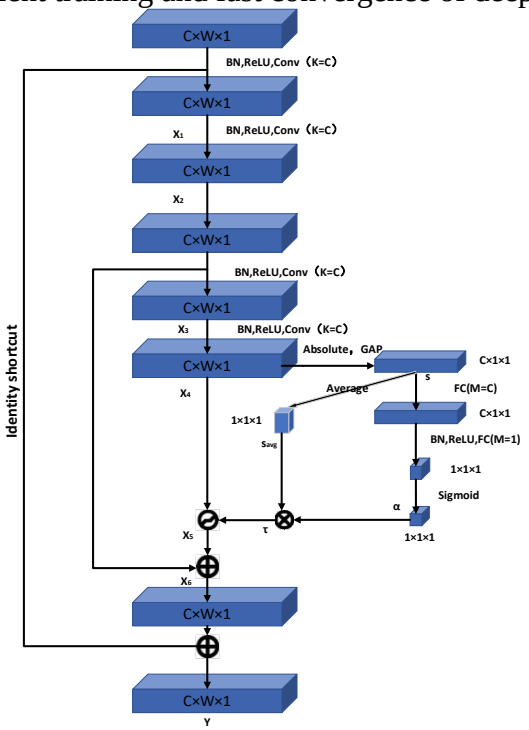

Figure 4: Structure Diagram of the DR-ResNet Module

The computation formula for the constructed DR-ResNet module is as follows:

The input X undergoes multiple convolutions, batch normalization (BN), and ReLU activation functions to generate the residual features X_4 . The computation formulas are shown in Equations (5) to (8):

$$X_1 = Conv(\mathrm{ReLU}(\mathrm{BN}(X))) \tag{3}$$

$$X_2 = Conv(\mathrm{ReLU}(\mathrm{BN}(X_1))) \tag{4}$$

$$X_3 = Conv(\mathrm{ReLU}(\mathrm{BN}(X_2))) \tag{5}$$

$$X_4 = Conv(\mathrm{ReLU}(\mathrm{BN}(X_3))) \tag{6}$$

The absolute value of the residual features X_4 is globally pooled (GAP) to generate a scalar, which represents the global strength of the features. The computation formula is shown in Equation (9):

$$s = GAP(Absolute(X_4)) \tag{7}$$

The scalar S is globally averaged pooled to obtain S_{avg}, and then passed through a fully connected layer, followed by batch normalization (BN), a ReLU activation function, another fully connected layer, and a sigmoid activation function to generate the scaling weight a for the channel. The computation formulas are shown in Equations (10) to (11):

$$s_{fc1} = FC_1(s) \tag{8}$$

$$a = \sigma(FC_2(ReLU(BN(s_{fc1})))) \tag{9}$$

The global average pooled S_{avg} is multiplied by a to obtain the final soft threshold τ :

$$\tau = a \cdot s_{avg} \tag{10}$$

The soft thresholding operation is applied to X_4 using the soft threshold τ to suppress irrelevant feature information. The formula for the soft thresholding operation is shown in Equation (13):

$$X_5 = sign(X_4) \cdot \max(|X_4| - \tau, 0) \tag{11}$$

The soft thresholded result X_5 is added to X_2 to obtain the output X_6.

$$X_6 = X_5 + X_2 \tag{12}$$

The input features are fused with the residual features to obtain the final output Y.

$$Y = X + X_6 \tag{13}$$

2.3 Loss Function

To calculate the loss for LFP signal classification, cross-entropy (CE) is used as the loss function,

which is defined as follows:

$$loss(input, target) = weight[target] \times (-input[target] + \log(\sum_{j} e^{input[j]})) \tag{14}$$

Where $input$ is a one-dimensional array processed by Softmax (the array consists of the predicted probability values for each label), and $target$ is the actual label. $input(j)$ represents the element at index j in the input array. $weight(target)$ is the actual weight, and the definition of $weight[target]$ is given by Equation (20).

$$weight[target] = \ln(\frac{1}{p(target)}) \tag{15}$$

Where $p(target)$ is the proportion of the label $target$ among all labels.

For the loss function, the Adam optimization algorithm with adaptive moment estimation is used, with a learning rate set to 5×10^{-4}, and all other parameters are kept at their default values. During each network training, the algorithm performs 20 optimization steps on all the training data, and then uses the validation set to obtain the system performance metrics.

3. Experiments and Comparative Results

3.1 Experimental Setup

The experiment is run in a Python environment on Ubuntu 18.04, built with PyTorch 1.0, and trained on an Nvidia GeForce RTX 3090 GPU with 24GB of memory.

3.2 Evaluation Metrics

In the experiment, recall (Recall), accuracy (Acc), and specificity (SP,) are used to evaluate the model performance. The formulas are shown in Equations (21), (22), and (23):

$$\text{Recall} = \frac{TP}{TP + FN}(\%) \tag{16}$$

$$\text{Accuracy} = \frac{TP + TN}{TP + FN + TN + FP}(\%) \tag{17}$$

$$\text{Specificity} = \frac{TN}{TN + FP}(\%) \tag{18}$$

Where TP, TN, FP, and FN represent the true positive samples, true negative samples, false positive samples, and false negative samples, respectively, when the classifier makes decisions about the class.

The Kappa coefficient, which can describe the overall performance of the system, is also calculated. The formulas are shown in Equations (24), (25), and (26)

$$Kappa = \frac{p_o - p_e}{1 - p_e} \tag{19}$$

$$p_o = \frac{TP + TN}{TP + TN + FP + FN} \tag{20}$$

$$p_e = \frac{(TP + FN) \cdot (TP + FP) + (TN + FP) \cdot (TN + FN)}{(TP + TN + FP + FN)^2} \tag{21}$$

3.3 Dataset

The experiment uses the publicly available dataset from Oxford University, which contains local field potentials from seven columns of patients. The electrode placement covers neural structures such as the STN, uncertain band, and thalamus from bottom to top. Bilateral recordings were conducted for 5 patients, generating a total of 12 hemispheres. Each electrode contains eight contact points, as shown in Figure 5, where contact points C1 and C2 collect signals from the subthalamic nucleus (STN), and C4, C5, C6, and C7 collect signals from the thalamus. The raw signals were filtered and segmented for processing.

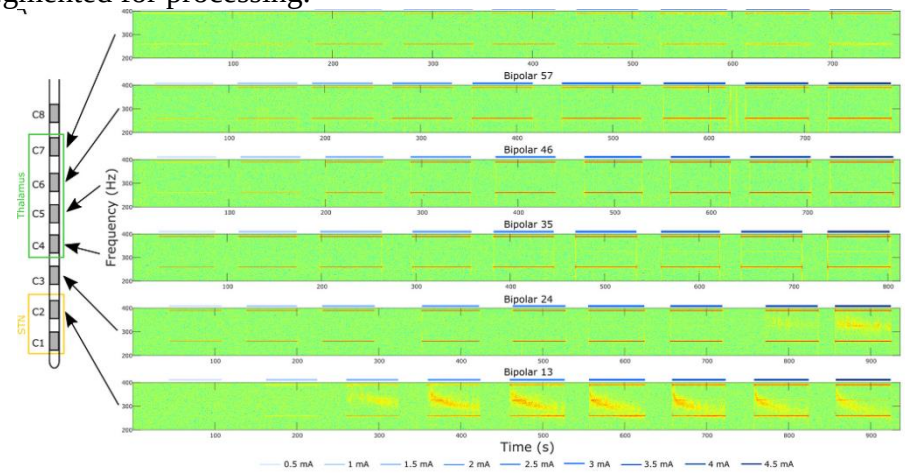

Figure 5: Electrode Stimulation Sites

To explore the impact of LFP signal length on the classification performance of the MSDR-ResNet model, the LFP signals were segmented into 0.5 seconds, 1 second, 3 seconds, and 5 seconds. The core objective of this experiment is to assess the model's classification performance on signals with different segment lengths, revealing the influence of segment length on feature capture. The experimental results are shown in Figure 6. The accuracy for 0.5-second, 1-second, 3-second, and 5-second LFP signals were 94.67%, 93.64%, 91.86%, and 91.32%, respectively. The recall rates were 94.52%, 92.52%, 90.43%, and 90.47%, respectively.

The experimental results indicate that the 0.5-second signal segment achieved the best classification performance, showing the highest accuracy, recall, and F1 score. The superior performance of the 0.5-second segment is primarily due to the fact that shorter time segments not only increase the training sample size but also capture more granular temporal variations, especially in the LFP signals of Parkinson's disease patients. These short time segments effectively reflect high-frequency, low-amplitude tremor activity, thereby capturing the rapid neural discharge patterns in Parkinson's disease. As a result, the model can more accurately identify tremor features when processing these segments, significantly improving classification accuracy.

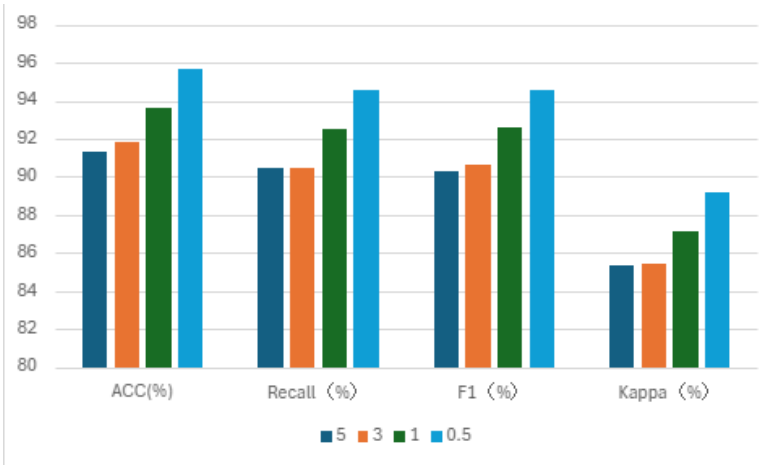

Figure 6: The Impact of Different Time Segments on Model Performance

3.4 Ablation Study

To assess the specific contribution of each module in the model, this study explores the impact of removing or replacing key modules (such as the multi-scale convolution path, deep residual shrinkage module, and SE attention mechanism) on overall performance. By comparing the model's accuracy under different experimental conditions, the role and importance of each module in the LFP signal classification task can be intuitively understood. The core steps of the ablation study to evaluate the performance of the improved residual neural network are as follows:

Removing the Multi-Scale Convolution Path: The multi-scale convolution path is replaced with two-path or four-path structures, and the performance changes in capturing features at different time scales are observed. This experiment validates the effectiveness of the multi-scale convolution path in capturing the multi-scale features of LFP signals:

Removing the Deep Residual Shrinkage Module: The DR-ResNet module is replaced with the standard residual module to evaluate the model's robustness under noise interference. This step aims to verify the role of the deep residual shrinkage module in noise suppression and improving classification accuracy.

Removing the SE Attention Mechanism: The SE module is removed, and the changes in the model's feature weighting are observed. By comparing the experimental results, the contribution of the SE module in enhancing important features and suppressing irrelevant ones is verified.

These ablation experiments provide detailed evidence for quantifying the specific contributions of each module in LFP signal processing. The results of the ablation study are shown in Table 1.

Table 1: Ablation Experiment of MSDR-ResNet

Two-Branch	Three-Branch	Four-Branch	DRSN	SE	ACC(%)
√					86.35
	√				89.63
		√			89.86
√			√		89.98
√			√	√	90.14
	√		√		93.66
	√		√	√	94.67
		√	√		93.03
		√	√	√	93.82

3.5 Comparison with Existing Models

To validate the feasibility of the MSDR-ResNet model, a comparative experiment was conducted between MSDR-ResNet and other existing models. The models compared include CNN, ResNet18, MRSN, CNN-LSTM, and CNN-GA-KNN, with accuracy, recall, F1 score, and Kappa coefficient as evaluation metrics. According to the data in the table, the MSDR-ResNet model achieved an accuracy of 94.67%, which is 6.71%, 5.04%, 6.04%, 4.09%, and 2.29% higher than the CNN, ResNet18, MRSN, CNN-LSTM, and CNN-GA-KNN models, respectively. Additionally, the recall, F1 score, and Kappa coefficient reached 94.52%, 94.58%, and 89.17%, all of which are higher than those of CNN, ResNet18, MRSN, CNN-LSTM, and CNN-GA-KNN models.

Table 2: Comparison of Accuracy across Different Models

	ACC	Recall(%)	F1(%)	Kappa(%)
CNN	87.96	87.91	87.83	75.69
ResNet18	89.63	89.10	86.61	79.22
MRSN	88.63	88.64	88.61	79.22
CNN-LSTM	90.58	89.54	89.32	80.59
CNN-GA-KNN	92.38	91.57	91.63	86.54
MSDR-ResNet	94.67	94.52	94.58	89.17

The experimental results, as shown in Table 2, indicate that the CNN model performs poorly in handling LFP signals, a complex time-series data, with an accuracy of only 87.96%. This limitation mainly arises from the fact that traditional CNN architectures typically use fixed-size convolutional kernels, which struggle to effectively capture the multi-frequency features in LFP signals, thus affecting the classification performance for Parkinson's disease signals. In contrast, the MSDR-ResNet model combines multi-scale convolution, the Deep Residual Shrinkage Network (DRSN) module, and the SE attention mechanism. This enables the model to not only capture multi-frequency features but also suppress noise and enhance key features, leading to more accurate classification. The MSDR-ResNet outperforms other models across multiple metrics, including accuracy, recall, F1 score, and Kappa coefficient.

In particular, the Kappa coefficient of MSDR-ResNet reached 89.17%, significantly higher than CNN's 75.69% and ResNet18's 79.22%. This indicates that the MSDR-ResNet model maintains high classification accuracy even in the presence of data imbalance or significant noise. In contrast, models like CNN-LSTM and CNN-GA-KNN, although performing well with time-series data, still fail to surpass the performance of MSDR-ResNet. These results suggest that the proposed model not only excels in feature extraction but also possesses superior noise suppression and generalization abilities, making it more effective in accurately identifying LFP signal features in Parkinson’s disease patients.

4. Conclusion

This paper proposes a Local Field Potential (LFP) signal classification method based on a multi-scale residual convolutional neural network (MSDR-ResNet). The method is capable of directly extracting features from raw LFP signals and performing classification. Cross-validation demonstrates its excellent adaptability to large-scale datasets, especially showcasing outstanding generalization ability when processing data from unknown subjects. Compared to other deep learning methods, this model achieves excellent classification performance without the need for complex data preprocessing and feature extraction steps. Furthermore, under sufficient computational resources, the multi-scale residual network can be deepened and trained with more data, theoretically leading to a more robust model with superior system performance.

References

[1] Wang X N. Study on physiological changes of footbridge nuclear power in rats with Parkinson's disease [D]. Shandong Normal University, 2020.

[2] Espay A J, Brundin P, Lang A E. Precision medicine for disease modification in Parkinson disease[J]. Nature reviews neurology, 2017, 13(2): 119-126.

[3] Alam M, Heissler H E, Schwabe K, et al. Deep brain stimulation of the pedunculopontine tegmental nucleus modulates neuronal hyperactivity and enhanced beta oscillatory activity of the subthalamic nucleus in the rat 6-hydroxydopamine model[J]. Experimental neurology, 2012, 233(1): 233-242

[4] Wang Jing, WANG Xuilian, Wang Jilei, et al. Analysis of firing patterns of pallidus neurons in rats with Parkinson's disease [J]. Journal of Stereotactic and Functional Neurosurgery, 2007, 20(6): 321-325. (in Chinese)

[5] LeWitt P A. New levodopa therapeutic strategies[J]. Parkinsonism & related disorders, 2016, 22: S37-S40

[6] Valsky D, Blackwell KT, Tamir I, Eitan R, Bergman H, Israel Z. Real-time machine learning classification of pallidal borders during deep brain stimulation surgery[J]. J Neural Eng. 2020 Jan 6; 17(1):016021.

[7] Mann JM, Foote KD, Garvan CW, Fernandez HH, Jacobson CE 4th, Rodriguez RL, Haq IU, Siddiqui MS, Malaty IA, Morishita T, Hass CJ, Okun MS. Brain penetration effects of microelectrodes and DBS leads in STN or GPi[J]. J Neurol Neurosurg Psychiatry. 2009 Jul; 80(7):794-7.

[8] Schuepbach W M M, Rau J, Knudsen K, et al. Neurostimulation for Parkinson's disease with early motor complications[J]. N Engl J Med, 2013, 368: 610–622.

[9] Boutet A, Madhavan R, Elias G J B, et al Predicting optimal deep brain stimulation parameters for Parkinson's disease using functional MRI and machine learning[J]. Nat Commun, 2021, 12: 1–13

[10] Zhang F, Wang F, Li W G, et al Relationship between electrode position of deep brain stimulation and motor symptoms of Parkinson's disease[J]. BMC Neurol, 2021, 21: 122

[11] Telkes I, Jimenez-Shahed J, Viswanathan A, Abosch A, Ince NF. Prediction of STN-DBS Electrode Implantation Track in Parkinson's Disease by Using Local Field Potentials[J]. Front Neurosci. 2016 May 9;10:198.

[12] J.D. Rolston, D.J. Englot, P.A. Starr, P.S. Larson, An unexpectedly high rate of revisions and removals in deep brain stimulation surgery: analysis of multiple databases[J]. Parkinsonism Related Disorders 33 (2016) 72–77.

[13] K. Rui, T. Maszczyk, A. An, Q. See, J. Dauwels, N. Kon, et al, A review on microelectrode recording selection of features for machine learning in deep brain stimulation surgery for Parkinson's disease[J]. Clinical Neurophysiology. 130 (1) (2019) 145–154.

[14] Farrokhi, Q.D. Buchlak, M. Sikora, N. Esmaili, M. Marsans, P. McLeod, et al, Investigating Risk Factors and Predicting Complications in Deep Brain Stimulation Surgery with Machine Learning Algorithms[J], World Neurosurgery 134 (2020) 468–481.

[15] Xiao L, Li C, Wang Y, et al. Automatic identification of sweet spots from MERs for electrodes implantation in STN-DBS[J]. International Journal of Computer Assisted Radiology and Surgery, 2021, 16(5): 809-818.

[16] Li C, Wang Y, Si W, Lin H, Zhang D, Cai X, Heng PA. Amplitude-frequency-aware deep fusion network for optimal contact selection on STN-DBS electrodes[J]. Science China Information Sciences. 2022 Apr;65(4):140404.

[17] Cao L, Li J, Zhou Y, Liu Y, Liu H. Automatic feature group combination selection method based on GA for the functional regions clustering in DBS[J]. Computer Methods and Programs in Biomedicine. 2020 Jan 1;183:105091.

[18] Peralta, Maxime, Quoc Anh Bui, Antoine Ackaouy, Thibault Martin, Greydon Gilmore, Claire Haegelen, Paul Sauleau, John SH Baxter, and Pierre Jannin. Sepaconvnet for localizing the subthalamic nucleus using one second micro-electrode recordings[C]. In 2020 42nd Annual International Conference of the IEEE Engineering in Medicine & Biology Society (EMBC), pp. 888-893. IEEE, 2020.

[19] Ciecierski, Konrad A., and Tomasz Mandat. Classification of DBS microelectrode recordings using a residual neural network with attention in the temporal domain[J]. Neural Networks,170(2024): 18-31.

[20] Karthick, P. A., Kai Rui Wan, Angela See An Qi, Justin Dauwels, and Nicolas Kon Kam King. Automated detection of subthalamic nucleus in deep brain stimulation surgery for Parkinson's disease using microelectrode recordings and wavelet packet features[J]. Journal of Neuroscience Methods 343 (2020): 108826.

[21] Hosny, Mohamed, Minwei Zhu, Wenpeng Gao, and Yili Fu. Detection of subthalamic nucleus using novel higher-order spectra features in microelectrode recordings signals[J]. Biocybernetics and Biomedical Engineering 41, no. 2 (2021): 704-716.

[22] Hosny, Mohamed, Minwei Zhu, Wenpeng Gao, and Yili Fu. A novel deep LSTM network for artifacts detection in microelectrode recordings[J]. Biocybernetics and Biomedical Engineering 40, no. 3 (2020): 1052-1063.

[23] Valsky, Dan, Odeya Marmor-Levin, Marc Deffains, Renana Eitan, Kim T. Blackwell, Hagai Bergman, and Zvi Israel. Stop! border ahead: Automatic detection of subthalamic exit during deep brain stimulation surgery[J]. Movement Disorders 32, no. 1 (2017): 70-79.

[24] Thompson, John A., David Lanctin, Nuri Firat Ince, and Aviva Abosch. Clinical implications of local field potentials for understanding and treating movement disorders[J]. Stereotactic and functional neurosurgery 92, no. 4 (2014): 251-

263.
[25] Priori, Alberto, Guglielmo Foffani, Lorenzo Rossi, and Sara Marceglia. Adaptive deep brain stimulation (aDBS) controlled by local field potential oscillations[J]. Experimental neurology 245 (2013): 77-86.
[26] Feldmann, Lucia K., Wolf-Julian Neumann, Katharina Faust, Gerd-Helge Schneider, and Andrea A. Kühn. Risk of infection after deep brain stimulation surgery with externalization and local-field potential recordings: twelve-year experience from a single institution[J]. Stereotactic and Functional Neurosurgery 99, no. 6 (2021): 512-520.
[27] Ozturk, Musa, Ilknur Telkes, Joohi Jimenez-Shahed, Ashwin Viswanathan, Arjun Tarakad, Suneel Kumar, Sameer A. Sheth, and Nuri F. Ince.Randomized, double-blind assessment of LFP versus SUA guidance in STN-DBS lead implantation: a pilot study[J]. Frontiers in Neuroscience 14 (2020): 611.
[28] Hosny, Mohamed, Minwei Zhu, Wenpeng Gao, and Yili Fu. A novel deep learning model for STN localization from LFPs in Parkinson's disease[J]. Biomedical Signal Processing and Control 77 (2022): 103830.
[29] Hosny, Mohamed, Minwei Zhu, Wenpeng Gao, and Ahmed M. Elshenhab. STN localization using local field potentials based on wavelet packet features and stacking ensemble learning[J]. Journal of Neuroscience Methods 407 (2024): 110156.
[30] Hosny, Mohamed, Minwei Zhu, Yixian Su, Wenpeng Gao, and Yili Fu. A novel deep recurrent convolutional neural network for subthalamic nucleus localization using local field potential signals[J]. biocybernetics and biomedical engineering 41, no. 4 (2021): 1561-1574.